NeuroImage 120 (2015) 143–153

Contents lists available at ScienceDirect

NeuroImage

journal homepage: www.elsevier.com/locate/ynimg

Towards high-quality simultaneous EEG-fMRI at 7 T: Detection and reduction of EEG artifacts due to head motion

João Jorge [a,b,*], Frédéric Grouiller [c], Rolf Gruetter [a,c,d], Wietske van der Zwaag [e,f], Patrícia Figueiredo [b]

[a] Laboratory for Functional and Metabolic Imaging, École Polytechnique Fédérale de Lausanne, Lausanne, Switzerland
[b] Institute for Systems and Robotics/Department of Bioengineering, Instituto Superior Técnico, Universidade de Lisboa, Lisbon, Portugal
[c] Department of Radiology, University of Geneva, Geneva, Switzerland
[d] Department of Radiology, University of Lausanne, Lausanne, Switzerland
[e] Biomedical Imaging Research Center, École Polytechnique Fédérale de Lausanne, Lausanne, Switzerland
[f] Spinoza Centre for Neuroimaging, Amsterdam, The Netherlands

ARTICLE INFO

Article history:
Received 21 April 2015
Accepted 7 July 2015
Available online 11 July 2015

Keywords:
Simultaneous EEG-fMRI
Ultra-high field
Head motion
Visual evoked potential
Adaptive filtering

ABSTRACT

The enhanced functional sensitivity offered by ultra-high field imaging may significantly benefit simultaneous EEG-fMRI studies, but the concurrent increases in artifact contamination can strongly compromise EEG data quality. In the present study, we focus on EEG artifacts created by head motion in the static B_0 field. A novel approach for motion artifact detection is proposed, based on a simple modification of a commercial EEG cap, in which four electrodes are non-permanently adapted to record only magnetic induction effects. Simultaneous EEG-fMRI data were acquired with this setup, at 7 T, from healthy volunteers undergoing a reversing-checkerboard visual stimulation paradigm. Data analysis assisted by the motion sensors revealed that, after gradient artifact correction, EEG signal variance was largely dominated by pulse artifacts (81–93%), but contributions from spontaneous motion (4–13%) were still comparable to or even larger than those of actual neuronal activity (3–9%). Multiple approaches were tested to determine the most effective procedure for denoising EEG data incorporating motion sensor information. Optimal results were obtained by applying an initial pulse artifact correction step (AAS-based), followed by motion artifact correction (based on the motion sensors) and ICA denoising. On average, motion artifact correction (after AAS) yielded a 61% reduction in signal power and a 62% increase in VEP trial-by-trial consistency. Combined with ICA, these improvements rose to a 74% power reduction and an 86% increase in trial consistency. Overall, the improvements achieved were well appreciable at single-subject and single-trial levels, and set an encouraging quality mark for simultaneous EEG-fMRI at ultra-high field.

Introduction

The simultaneous acquisition of scalp electroencephalography (EEG) and functional magnetic resonance imaging (fMRI) can yield valuable insights into the dynamics of brain function (Babiloni et al., 2004; Gotman and Pittau, 2011; Jorge et al., 2014). A fundamental line of development for fMRI has been the pursuit of higher magnetic field strengths, which leads to super-linear gains in functional sensitivity (van der Zwaag et al., 2009), that can be traded for increased spatial resolution (Da Costa et al., 2011; Yacoub et al., 2008). Unfortunately, however, simultaneous EEG-fMRI acquisitions at ultra-high field suffer from various undesirable interactions that can degrade data quality and potentially compromise subject safety (Dempsey et al., 2001; Neuner et al., 2014). Safety concerns have been effectively moderated (Lemieux et al., 1997; Noth et al., 2012), and although EEG components can reduce the signal-to-noise ratio (SNR) of MR images, numerous studies have found that losses in temporal SNR remain acceptable for fMRI, even at ultra-high field strengths with fairly high electrode densities (Jorge et al., 2015; Luo and Glover, 2012; Mullinger et al., 2008b). In contrast, the artifacts induced in EEG recordings by the magnetic fields used in fMRI can surpass the signals of interest by several orders of magnitude, and severely compromise data quality (Allen et al., 2000; Debener et al., 2008). This is currently the most limiting obstacle for high-quality EEG-fMRI acquisitions, particularly at higher field strengths such as 7 T.

EEG artifacts are mainly created by electromagnetic induction in the loops formed by the EEG leads, which occur whenever the existing magnetic field changes in time, or when loop geometry is changed relative to the field (Yan et al., 2009). The strongest contributions are generally due to the fast-switching gradient fields applied for image encoding (Allen et al., 2000). Cardiac activity can also cause large artifacts through

* Corresponding author at: Laboratory for Functional and Metabolic Imaging, LIFMET-CIBM, Station 6, École Polytechnique Fédérale de Lausanne, CH-1015 Lausanne, Switzerland.
E-mail address: joao.jorge@epfl.ch (J. Jorge).

http://dx.doi.org/10.1016/j.neuroimage.2015.07.020
1053-8119/

various mechanisms, including bulk head motion prompted by the arrival of the ejected blood, scalp expansion due to arterial pulsation, and Hall effects occurring in the moving blood — altogether known as pulse artifacts (Mullinger et al., 2013; Yan et al., 2010). Given their importance, a considerable amount of work has been dedicated to the study of gradient and pulse artifacts, and the development of strategies for their minimization (Mullinger and Bowtell, 2011). The inherent reproducibility of gradient artifacts renders them suitable for correction based on average artifact subtraction (AAS) (Allen et al., 2000), guided by image acquisition triggers obtained from the scanner, and possibly complemented with optimal basis set (OBS) methods (Niazy et al., 2005). The cyclic nature of cardiac activity has also motivated a widespread use of AAS and OBS-based approaches for pulse artifact correction (Allen et al., 1998; Niazy et al., 2005), in this case guided by triggers from a separate cardiac trace such as the electrocardiogram (ECG).

Given their dependence on Faraday's law of induction (Yan et al., 2009), many EEG artifact contributions scale with the amplitude of the static magnetic field B_0, and previously less relevant sources can attain important roles in data degradation at 7 T. These include mechanical vibrations propagated from the scanner environment, particularly due to the Helium (He) compression systems (Mullinger et al., 2008a) and patient ventilation (Nierhaus et al., 2013). Spontaneous head motion in B_0 can likewise become highly problematic, with visible artifact contributions even for experienced, steady subjects, and very limiting data degradation for less compliant subjects. Compared to gradient and pulse artifacts, considerably less work has been devoted to these contributions. Vibration-induced noise can be avoided by switching off the associated sources during acquisition, when possible (Mullinger et al., 2008a; Nierhaus et al., 2013), and certain EEG hardware modifications have been proposed to minimize its incidence (Jorge et al., 2015). The periodic structure of He coldhead contributions, in particular, has motivated a few novel data-based correction approaches as well (Kim et al., 2015; Rothlubbers et al., 2013). Spontaneous head motion, however, is highly unpredictable, and while periods of important movement can often be identified by visual inspection and excluded, more subtle and widespread contributions can prove very hard to discern from true EEG patterns, even on simplified data decompositions such as those given by independent component analysis (ICA) (Arrubla et al., 2013; Debener et al., 2007). To address this challenge, a few groups have instead explored the use of dedicated motion sensors, recorded along with EEG-fMRI, which can be used to estimate and remove motion artifacts from the EEG data (Hill et al., 1995). At 1.5 T, Bonmassar et al. (2002) used a piezoelectric transducer to record motion information, and applied an adaptive denoising technique based on Kalman filtering to reduce both spontaneous motion and the motion-related component of the pulse artifact. In a later study at 3 T, Masterton et al. (2007) proposed the use of multiple sensors based on carbon wire loops, distributed over the EEG cap and sensitive to magnetic induction effects. These sensors were shown to provide richer information for motion and pulse artifact estimation, with clear benefits for the identification of epileptiform activity (Abbott et al., 2014). More recently, so-called reference layer methods have been explored, where EEG-like electrodes are distributed on a conductive layer on top of the EEG cap, but isolated from the scalp, recording only induction effects. These approaches aimed at both motion and pulse artifacts (Luo et al., 2014) and even gradient artifacts (Chowdhury et al., 2014), at the cost of requiring larger numbers of sensors.

While the use of dedicated sensors for artifact monitoring and reduction has shown clear benefits for EEG data quality (Chowdhury et al., 2014; Flanagan et al., 2009; Luo et al., 2014), these approaches have so far not achieved widespread use. This is possibly due to the need for additional recording equipment for the sensors (including amplification, synchronization with EEG acquisition, etc.), as well as other customized elements (electrodes, gel layers), altogether increasing the cost and complexity of acquisition setups. This is a highly disadvantageous situation given the unique potential of these approaches for motion artifact reduction, with crucial importance at higher field strengths. In the present study, we propose a novel approach for motion artifact recording and EEG data denoising, and assess the benefits of this methodology for simultaneous EEG-fMRI in humans at 7 T. Artifact detection was performed with a simple and non-permanent modification of a commercial EEG cap, where four electrodes were isolated from the scalp and connected to the reference electrode via added resistors, measuring only magnetic induction effects. Several analysis approaches were investigated for optimal use of the sensor recordings in EEG signal correction, including: (I) a study of the combination of motion and pulse artifact correction techniques, (II) the development of different techniques for offline motion artifact correction, along with an assessment of artifact contributions at 7 T, and (III) the integration of motion artifact correction with ICA-based denoising. Overall, data quality improvements were evaluated in terms of EEG power reduction and increases in sensitivity to visual evoked potentials (VEP), particularly at a single-trial level.

Theory

Here, the mechanisms underlying EEG artifact generation due to head motion are described, to provide a theoretical basis for the development of effective correction strategies.

Motion artifact generation

EEG artifacts due to head motion in the magnetic field $\vec{B}_0$ can be described by Faraday's law of induction (Yan et al., 2010), which states that changes in the magnetic flux passing through the loop formed by an EEG channel C_i with the reference channel, C_{ref}, will induce an electromotive force ξ_i in the corresponding loop given by:

$$\xi_i(t) = -\frac{d\Phi_\Sigma}{dt}(t) = -\frac{d}{dt}\int_\Sigma \vec{B}_0\left(\vec{r},t\right)\cdot\vec{N}\left(\vec{r},t\right)d\Sigma \tag{1}$$

where Φ_Σ is the magnetic flux through the surface Σ enclosed by the loop (Fig. 1a), and $\vec{N}$ is the unitary normal vector to the surface, at each position $\vec{r}$ and instant t. This is an approximated description where the current path between C_i and C_{Ref} is treated as a linear path along the scalp surface (a more rigorous approximation would involve modeling the volume conduction properties of the head (Yan et al., 2009)). Additionally, flux contributions from wire segments leaving the cap surface are assumed to be minimal, as can be achieved by adequate cable optimization (Jorge et al., 2015). If $\vec{B}_0$ is spatially homogenous, stationary and parallel to the z-axis, and assuming rigid-body motion, Eq. (1) can be simplified to:

$$\xi_i(t) = -B_0\int_\Sigma \frac{d}{dt}N_z\left(\vec{r},t\right)d\Sigma \tag{2}$$

where N_z is the z-component of the surface normal vector. It follows from Eq. (2) that only rotations along the x- and y-axis can produce induction effects, as $N_z(\vec{r},t)$ does not change with translations or with rotations along the z-axis. Under the rigid-body assumption, the evolution of $N_z(\vec{r},t)$ with x- and y-axis head rotations (globally described by angles ϕ and θ, respectively) can be written as:

$$N_z\left(\vec{r},t\right) = \sin\theta N_x^0\left(\vec{r}\right) - \sin\phi\cos\theta N_y^0\left(\vec{r}\right) + \cos\phi\cos\theta N_z^0\left(\vec{r}\right) \tag{3}$$

where N_x^0, N_y^0, and N_z^0 are the original components of the normal vector. Inserting this decomposition in Eq. (2) and applying the temporal derivative, we obtain an expression of the form:

$$\xi_i(t) = F_i(\phi(t),\theta(t))\frac{d\phi}{dt}(t) + G_i(\phi(t),\theta(t))\frac{d\theta}{dt}(t) \tag{4}$$

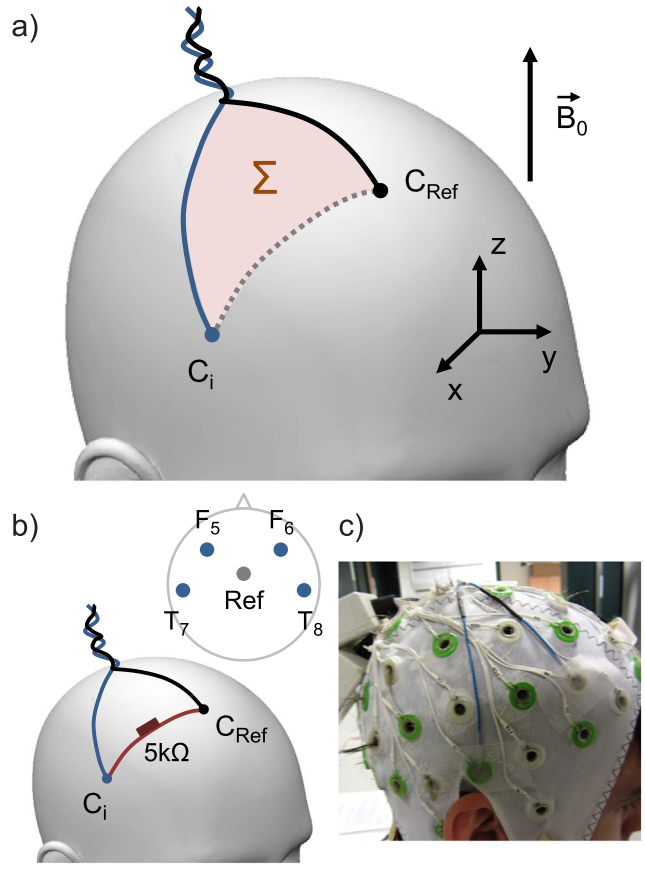

Fig. 1. Schematics of EEG motion artifact generation and detection. a) Representation of a loop formed by a given EEG channel C_i with the reference C_{Ref}, covering an area Σ on the scalp surface; the static magnetic field $\vec{B}_0$ is depicted along the *z*-direction. b) Representation of the non-permanent cap modifications employed for motion artifact detection: each of the selected channels (T7, T8, F5 and F6) was isolated from the scalp and given a direct connection to the reference via a 5 kΩ resistor. c) The modified cap after preparation on a human subject.

where F_i and G_i are surface integrals of linear combinations of sine and cosine functions of ϕ and θ, weighted by N_x^0, N_y^0, and N_z^0 at each position $\vec{r}$. The potential difference created between C_i and C_{Ref} will then be proportional to ξ_i, and is measured in addition to the true, physiological EEG signal.

The structure of Eq. (4) suggests that this contribution can be approximated by a linear model with two degrees of freedom, $d\phi/dt$ and $d\theta/dt$, weighted by temporally-varying coefficients, $F(\phi, \theta)$ and $G(\phi, \theta)$. While the coefficients are channel-specific, the two rotations are common to all loops in the rigid body. This thus motivates the use of loop-based motion sensors, sensitive to similar induction effects, and the use of adaptive linear models to combine their timecourses and estimate the artifact contributions affecting actual EEG channels.

Motion artifact correction

We consider a recorded signal $y = s + m$, where s is the EEG signal of interest and m is a motion artifact timecourse. The two components are assumed to be uncorrelated. Based on a set of motion sensor signals x_i, recorded along with y, the timecourse m is then modeled as a linear combination of the sensors, weighted by time-varying coefficients w_i:

$$m(t) = \sum_i w_i(t) x_i(t). \tag{5}$$

These coefficients can then be estimated through various approaches, as described below.

Linear regression with basis set coefficients (BLS)

The model described by Eq. (5) can be made parametric by defining the coefficients w_i as linear expansions of appropriate basis functions b_j (Huang et al., 2002):

$$w_i(t) = \sum_j a_{i,j} b_j(t). \tag{6}$$

The introduction of Eq. (6) in Eq. (5) leads to a new linear model with fixed coefficients $a_{i,j}$ for each product $b_j x_i$, which can then be estimated analytically using an ordinary least-squares approach.

Sliding-window weighted least squares (WLS)

In the model described by Eq. (5), the coefficients w_i can be determined at each instant t by considering a local time window of the data centered on t, V_t, and applying weighted least-squares (WLS) linear regression to that segment (Fan and Zhang, 2000; Hoover et al., 1998). In this sense, the least-squares cost function to minimize is defined as:

$$E(w,t) = \sum_{\tau \in V_t} \Omega(\tau - t)\left(y(\tau) - \sum\nolimits_i w_i x_i(\tau)\right)^2 \tag{7}$$

where Ω is a weight function that can be chosen to attribute more importance to instants closer to t.

Multi-channel recursive least squares (M-RLS)

Originally proposed for active noise control in audio applications (Bouchard and Quednau, 2000), multi-channel recursive least-squares (M-RLS) is a real-time estimation method based on Kalman filtering, which has already been successfully applied to EEG data with loop-based motion sensors (Masterton et al., 2007). In this method, the linear model includes the original sensor timecourses x_i along with time-shifted versions, forming a finite impulse response (FIR) filter. For each instant t, the fitting weights w_i are updated from $t - 1$ to produce the best estimate of $m(t)$, combining FIR-filtering, regressor decorrelation and least-squares fitting within the same update. A scalar parameter λ controls the adaptability of the algorithm.

Methods

This study was approved by the institutional review board of the local ethics committee, and involved the participation of 6 healthy volunteers (20 ± 2 years old, 5 male/1 female), who provided written informed consent. Volunteers were asked to remain as still as possible during acquisitions.

Data acquisition

Simultaneous EEG-fMRI acquisitions were performed on an actively-shielded Magnetom 7 T head scanner (Siemens, Erlangen, Germany), with 680 mm bore diameter (Magnex Scientific, Oxford, UK). The scanner was equipped with a head gradient set and an 8-channel transmit/receive head loop array (Rapid Biomedical, Rimpar, Germany). Functional images were acquired using a 2D multi-slice gradient-echo EPI sequence, with 25 axial slices per volume, 1.5 × 1.5 × 1.5 mm^3 spatial resolution, TR/TE = 2000/25 ms, α = 78°, 2×-GRAPPA acceleration, 7/8 partial Fourier imaging and sinusoidal readout. The scanner He coldheads were kept in function at all times, while patient ventilation and room lights were switched off.

EEG data were recorded using two 32-channel BrainAmp MR Plus amplifiers (Brain Products, Munich, Germany) and a customized BrainCap MR model (EasyCap, Herrsching, Germany). The cap contained 64 Ag/AgCl ring-type electrodes ("multitrodes") arranged following an extended 10–20 system, and was designed with shortened copper leads. Each lead contained a 5 kΩ resistor near the electrode and another inside the connector. One of the 64 electrodes was placed on

the back of the subject for ECG recording. Abralyte gel (EasyCap) was used to reduce electrode impedances. The cap connectors were linked to the EEG amplifiers via two 12 cm bundled cables, with the amplifiers placed just outside the head array (Jorge et al., 2015). After bandpass filtering (0.016–250 Hz) and digitization (0.5 μV resolution), the EEG signals were transmitted to the control room via fiber optic cables. Sampling was performed at 5 kHz, synchronized with the scanner 10 MHz clock. Scanner triggers marking the onset of each fMRI volume were also recorded. All EEG artifact corrections were performed offline, after acquisition, as described in the EEG data analysis section.

Motion sensors

In this setup, four of the EEG electrodes (T7, T8, F5 and F6) were adapted to serve as motion artifact sensors. For this set, each electrode was isolated from the scalp and given a direct connection to the reference electrode (FCz) via a copper wire fitted with a non-magnetic 5 kΩ resistor (Vishay, Malvern PA, USA) (Fig. 1b). Connections were performed in a non-permanent way: the selected electrodes were isolated from the scalp by placing plastic tape underneath, and then filled with gel within the ring; the connecting wires terminated in small Ag/AgCl probes (Warner Instruments, Hamden, CT, USA) that were dipped in the gel (Fig. 1c), allowing conduction between the four electrodes and the reference electrode (which was not isolated and kept functioning as normal). Given the high input impedance of the amplifiers, current flows along the wires due to neuronal activity can be considered negligible (Yan et al., 2009), and as such the electric potential measured by each of the adapted electrodes will be equal to the potential at the reference, added by magnetically-induced fluctuations occurring in the loop. As the system records EEG signals as the difference in potential between each channel and the reference, by design, these four channels will then monitor essentially magnetic induction effects — including gradient, pulse, vibration and spontaneous motion artifacts. For each subject, the sensor connections were placed after minimizing the impedances for the other electrodes, adding approximately 5 min of preparation time.

Functional paradigm

Each of the 6 volunteers underwent a 5-minute VEP run using reversing-checkerboard stimuli. Checkerboards were presented during ten 10 s blocks at a reversal frequency of 3.35 Hz (totaling 33 reversals per block), followed by 20 s of rest (fixation). The 7°-wide field of view featured a red cross at its center at all times, with slight shifts in color occurring twice per block at random time delays. Subjects were instructed to focus on the cross and report color shifts via a button press. Checkerboards were presented at 50% contrast, with an equivalent average luminance to the fixation periods. As the stimulation was performed using an LCD projector, a StimTracker box (Cedrus Corporation, San Pedro, CA, USA) equipped with a photodiode sensor was used to record the precise timing of checkerboard reversals.

EEG data analysis

Data analysis was performed in Matlab using routines developed in-house. All functional runs underwent an initial preprocessing pipeline, and were then studied in three distinct parts, addressing (I) the integration of motion and pulse artifact correction, (II) the optimization and comparison of motion correction approaches, and (III) the integration of motion correction with ICA denoising.

Data preprocessing

All recorded channels, including the motion sensors, underwent the same preprocessing routine. For each run, based on the recorded fMRI volume triggers, slice triggers were obtained by splitting each volume interval in 25 equal segments, and fine-tuned by maximizing inter-slice correlations on a 10×-upsampled EEG channel (Niazy et al., 2005). Gradient artifacts were then corrected slice-by-slice via AAS (Allen et al., 2000); each slice was corrected by subtracting an average over 100 slice samples (50 from the preceding and 50 from the following slices), with jittered steps of 8–13 slices separating the selected samples. These steps permitted sufficient spacing between samples to avoid removing lower-frequency EEG activity (Niazy et al., 2005), and yielded a balanced distribution of samples relative to the visual stimulation cycle (3.35 Hz), mitigating phase-locking effects.

Cardiac triggers were estimated from the ECG channel and fine-tuned by another correlation–maximization approach, using a combination of EEG channels where pulse artifacts were most prominent. Based on these triggers, pulse artifacts were reduced via AAS, subtracting each instance of an average over the closest 50 pulse samples (25 of the preceding and 25 of the following cardiac cycles). AAS was chosen for this step because each artifact instance is corrected with a fixed linear combination of its neighbors, which is the same for every channel (both EEG and motion sensors), thus preserving the linearity relationships of Eq. (4). This would not hold for certain approaches such as OBS, where each instance is corrected by a local fit (not a subtraction) of basis functions, which is differently biased by the ongoing motion artifacts and EEG fluctuations of each channel.

Following gradient and pulse artifact correction, EEG data were downsampled to 250 Hz, and bad channels were identified (2–5 per subject) and replaced by weighted averages of 3–4 of the neighboring electrodes. Each functional run was also inspected based on its global field power (GFP) timecourse, and periods displaying strong GFP peaks were manually excluded from all subsequent analyses (a total of approximately 20–40 s per 5-minute run).

Part I: pulse and motion artifact correction

Previous studies have assumed the pulse artifact to be mainly caused by bulk head motion, relying on sensor information to correct both pulse and spontaneous motion artifacts (Bonmassar et al., 2002; Masterton et al., 2007). Here, the potential benefits of combining motion artifact correction with a dedicated pulse artifact correction step (AAS-based, as described in the Data preprocessing section), at 7 T, were investigated. The original data were preprocessed in two versions, one with and another without pulse artifact correction. Both datasets underwent temporal highpass-filtering (1 Hz) and then motion artifact correction with M-RLS, implemented exactly as proposed in Masterton et al. (2007) (35 shifts for the FIR kernel with 2×-downsampling, $\lambda = 1–10^{-8}$).

Part II: optimization of motion artifact correction

This part focused on the comparison of different approaches for optimal sensor-based motion artifact correction. Based on the results from part I, pulse artifact correction was included in data preprocessing. Temporal bandpass filtering was also applied, set at 2–120 Hz for EEG data and 2–30 Hz for the motion sensors. The choice of a highpass cutoff of 2 Hz was motivated by preliminary tests showing that increasing the cutoff frequency improved motion artifact estimation, likely due to reduced biases from slow-drift contributions; this compromise comes at the cost of excluding EEG information from part of the delta band, but did not affect VEP morphology (Widmann et al., 2015). The choice of a lowpass cutoff of 30 Hz for the motion sensors was again based on insights from part I, pointing that this is the relevant frequency band for motion contributions. Motion correction was based on the linear model of Eq. (5), and explored the three approaches introduced in the Motion artifact correction section: BLS, sliding-window WLS and M-RLS. In all cases, the model regressors x_i included the 4 original sensors and a set of shifted versions of their timecourses, to produce a subject-specific FIR kernel (Bonmassar et al., 2002). The number and spacing of the shifts were optimized by testing multiple models with linear fits to the data (assuming constant weights w_i), and then comparing the respective adjusted coefficients of determination (R^2_{adj}), as well as the impact on visual response amplitude. R^2_{adj} is a goodness-of-fit measure that is independent of the number of regressors in a model, and is

thus particularly suitable for model comparison (Jorge et al., 2013). As all approaches were designed for offline correction, both positive and negative shifts could be included in the models — this was confirmed to produce better results than including only shifts from the past, as in real-time correction.

BLS: for this approach, three basis sets were tested to model the time-varying coefficients w_i, all designed to model smooth fluctuations: (i) a discrete cosine transform expansion (DCT), (ii) a full Fourier series expansion with an initial linear slope term, and (iii) a cardinal cubic B-spline set (Huang et al., 2002). The optimal expansion degree for each case was estimated by a similar empirical procedure to the one used for FIR kernel optimization.

Sliding-window WLS: for this approach, a Gaussian distribution was chosen as weight function for the sliding window, with its full width at half maximum (FWHM) controlling the temporal adaptability of the estimation. Preliminary tests yielded a value of 60 s as a good compromise between adaptability and robustness.

Offline M-RLS (oM-RLS): this approach was based on the method described by Masterton et al. (2007), with a number of modifications that took advantage of the choice for post-acquisition data correction: (1) both forward and backward shifts were included in the FIR kernel, optimized as described above; (2) the coefficients w_i were updated for every time instant; and (3) the coefficient timecourses were estimated with a double passage, where the iterations were first performed forwards in time, from the beginning to the end of the timecourse, and then backwards. This yielded a cleaner estimation for the starting periods, where the initial passage is not accurate since the coefficients take a certain time to converge from the initial set value ($w_i(0) = 0$) to the least-squares solution (see Supplementary Fig. 1 for an example). The adaptability parameter λ was kept at a value of $1–10^{-8}$, as in Masterton et al. (2007).

Besides the comparison of the three correction approaches, an additional characterization of the different artifact contributions to EEG signal power was performed in this part, based on the results from oM-RLS correction. For each subject, the EEG data resulting from three stages of the correction pipeline were considered: gradient artifact-corrected, gradient + pulse artifact-corrected, and finally gradient + pulse + motion artifact-corrected. At each stage, an estimate of the signal variance was obtained for each channel, and then averaged across channels. The decreases in variance across stages were then computed, as an estimate of the fraction of total signal variance expressed by each of the targeted sources (assuming all sources are uncorrelated).

Part III: motion artifact correction and ICA

ICA is a powerful exploratory technique that is often used in EEG data denoising (Arrubla et al., 2013; Eichele et al., 2005; Jorge et al., 2015). In this last section, we compared the performance of motion artifact correction based on motion sensors with an approach based on ICA denoising, and investigated the potential benefits of combining the two techniques. As in part II, data preprocessing included pulse artifact correction and temporal bandpass filtering (2–120 Hz for EEG data, 2–30 Hz for the motion sensors). Data were then corrected based on the motion sensors, ICA, or a combination of motion artifact correction followed by ICA denoising. The approach here chosen for motion artifact correction was oM-RLS (as discussed in the Motion artifacts and ICA section). ICA decomposition was performed with the extended infomax algorithm (Lee et al., 1999), imposing statistical independence in the temporal dimension. The resulting components were then reviewed based on their topography, trial-average response and trial-by-trial consistency (Arrubla et al., 2013). Components found to be clearly not related to the visual response (pulse and motion artifacts/residuals, eye-movement artifacts, etc.) were marked and excluded from subsequent data reconstruction. Additionally, an alternative ICA-based approach was tested where the motion sensor timecourses were included as additional channels in the ICA decomposition, and reconstruction was performed after manually rejecting components with strong projection weights in the motion channels. This approach guided by motion information was termed motion-integrated ICA (miICA).

Performance measures

For the three main parts of data analysis (I–III), the performance of the different correction approaches under study was assessed based on EEG signal power and VEP single-trial consistency. EEG power was computed for each channel via fast Fourier transform of the entire timecourse, and estimated for the full frequency band (1–125 Hz), as well as for specific bands delta (1–4 Hz), theta (4–8 Hz), alpha (8–12 Hz), beta (12–30 Hz) and gamma (30–100 Hz), in part I. For part I, relative power reductions obtained with correction were also estimated in dB as $10\ \log_{10}(P_f/P_i)$ (with P_i and P_f being the power before and after correction, respectively), for direct comparison with results from Masterton et al. (2007) at 3 T. VEP trial consistency was estimated after bandpass filtering (3–40 Hz) and re-referencing to the channel average, and involved computing the trial-average response in each channel, and then performing a least-squares fit of the average to each single trial. This yielded a Z-score of the fit per trial and per channel; the scores of all trials from occipital channels (Oz, 1, 2 and POz, 3, 4, 7, 8) were then averaged together, to yield a single Z-score per subject. The more restrictive filtering range of 3–40 Hz employed for this estimation was previously confirmed not to affect the average VEP morphology, while leading to more accurate single-trial fits. While signal power provides a more direct measure of the impact of denoising approaches on signal variability, VEP trial consistency is more informative of changes in response sensitivity due to artifact reduction, including potential effects of over-correction (since, under the assumption that the motion timecourses are uncorrelated with the visual responses, over-corrections will affect the different trials differently, and thereby reduce trial consistency). It should nevertheless be noted that this measure is only intended to monitor the effects of artifact correction, as it does not differentiate the natural variability of brain responses (Debener et al., 2006) from the variability introduced by the artifacts. For both measures, the values obtained with each correction approach were then compared via paired t-tests across subjects, assuming a maximum p-value of 0.05 for statistical significance. Relative variations in power and trial consistency reported in the text are shown as average ± standard error across subjects. In part III, the quality improvements obtained with the optimal correction approach were further analyzed by direct observation of its effects on the trial-average and single-trial responses of individual subjects.

Results

Tests conducted with the motion sensors showed no discernible contamination of the motion timecourses with neuronal activity. In particular, for EEG recordings performed outside the scanner on a volunteer at rest, signal power in the motion channels was below 1.4 μV^2, compared to an average across the scalp of 41 ± 28 μV^2 for the EEG channels. A power peak in the alpha band was clearly identifiable in most EEG channels, including those adjacent to the reference electrode (Fz, Cz, FC1, FC2), but not on the motion sensors; accordingly, the temporal correlation between motion timecourses and EEG timecourses was, on average, 0.04 ± 0.02. The impact of the sensor modification on fMRI data quality was found negligible, adding no visible susceptibility artifacts to the images; a white matter temporal SNR of 19 ± 1 was estimated for this subject group, whereas a value of 17 ± 1 had been obtained in a previous study with a group of similar size and the same MRI acquisition parameters, using a non-modified EEG setup (see Jorge et al. (2015) for further details).

Part I: pulse and motion artifact correction

The impact of motion artifact correction with M-RLS was well visible in both the temporal and spectral domains of each subject dataset, even

when pulse artifact correction had been applied beforehand with AAS (see Supplementary Fig. 2 for an example). The three correction approaches (AAS, M-RLS and AAS + M-RLS) also brought appreciable changes to VEP morphologies across the scalp for each subject (see example in Supplementary Fig. 3). To evaluate the impact of AAS, M-RLS and AAS + M-RLS, the corrected and uncorrected data were compared in terms of signal power and VEP trial consistency. Across delta, theta, alpha and beta bands, all three approaches produced statistically significant reductions in signal power, with M-RLS performing more effectively than AAS, but the combination of AAS followed by M-RLS achieving the largest power reductions (Fig. 2a). For the gamma band, no significant changes in power were found for any of the approaches. Compared to results obtained at 3 T using a similar M-RLS implementation (Masterton et al., 2007), the power attenuation achieved (without prior pulse correction) was approximately 1.5× larger in the delta band, 2.3× larger in the theta and alpha bands, and 4.8× larger in the beta band, at 7 T (Fig. 2b).

Across subjects, full-band EEG signal power achieved its lowest average value with the combination of AAS and M-RLS, corresponding to a 91 ± 1% reduction relative to the uncorrected data (Fig. 3a). The power achieved with the combined approach was significantly lower than with each method separately. An equivalent outcome was found for VEP trial consistency, with the combination of AAS and M-RLS yielding an average increase of 55 ± 5% in consistency Z-score (Fig. 3b). The value achieved was significantly higher than with AAS alone, and also superior to M-RLS alone, although not reaching significance ($p = 0.12$). Regarding full-band power distributions across the scalp, the original (preprocessed) data exhibited a strong concentration of power at the most lateral electrodes, along with a more moderate presence at occipital electrodes (Fig. 3c). Across the scalp, the use of AAS appeared to have a higher impact on occipital electrodes, while M-RLS produced stronger changes in more lateral electrodes. The combination of both approaches led to the most balanced, radial power distribution (centered at the reference electrode). The power attenuation achieved by M-RLS, after AAS correction, was confirmed to be strongest at more lateral regions (Fig. 3c, right).

Part II: optimization of motion artifact correction

Regarding model optimization, the preliminary tests performed for each subject, iterated in steps of 5 added shifts, indicated optimal kernel sizes of 11–61 regressors per motion sensor (41, 11, 61, 41, 61 and 21 for subjects 1–6, respectively), centered at $\Delta t = 0$ and spanning both positive and negative shifts in steps of 4 time samples (i.e., −80, −64, −48, −32, −16, 0, +16, +32, +48, +64, +80 ms for subject 2, for example). Regarding the BLS approach, the three bases tested yielded very similar results for this subject group, and as such only the simplest, DCT, was considered for further comparisons. For this basis set, an expansion up to 2nd degree (cosine period equal to the total timecourse length) showed a good compromise between temporal adaptability and model size.

Following optimization, the different approaches developed for motion artifact correction (DCT-based BLS, WLS and oM-RLS) were applied to the data and then compared in terms of signal power and trial consistency. All three approaches achieved statistically significant power reductions of 62 ± 4% (DCT), 63 ± 4% (WLS) and 61 ± 4% (oM-RLS), relative to the preprocessed, pulse-corrected data (Fig. 4a). Analogously, in trial consistency, these approaches led to significant improvements of 58 ± 15% (DCT), 57 ± 14% (WLS) and 62 ± 17% (oM-RLS) in consistency Z-score (Fig. 4b). No significant differences between the three correction approaches were found for either measure. Alongside group-average effects, motion artifact correction produced clear improvements on visual response quality at the level of individual subjects — a detailed description is given below (Part III: motion artifact correction and ICA section and Fig. 7). The characterization of signal variance contributions yielded consistent results across the subject group, with pulse artifact contributions explaining 81–93% of the total variance, while spontaneous motion artifacts and actual neuronal activity (plus residual artifacts) expressed more moderate contributions of 4–13% and 3–9%, respectively (Fig. 5). Spontaneous motion contributions were comparable or superior to neuronal contributions in 5 of the 6 subjects.

Part III: motion artifact correction and ICA

To evaluate the performance of ICA, miICA and oM-RLS artifact correction, the corrected and uncorrected data of all subjects were analyzed in terms of signal power and VEP trial consistency. On average, full-band EEG power was reduced by 53 ± 5% with miICA, 60 ± 4% with ICA, 61 ± 4% with oM-RLS, and 74 ± 3% with oM-RLS followed by ICA, relative to the preprocessed pulse-corrected data (Fig. 6a). The EEG power achieved with the combined approach was significantly lower than with individual methods. Regarding VEP trial consistency,

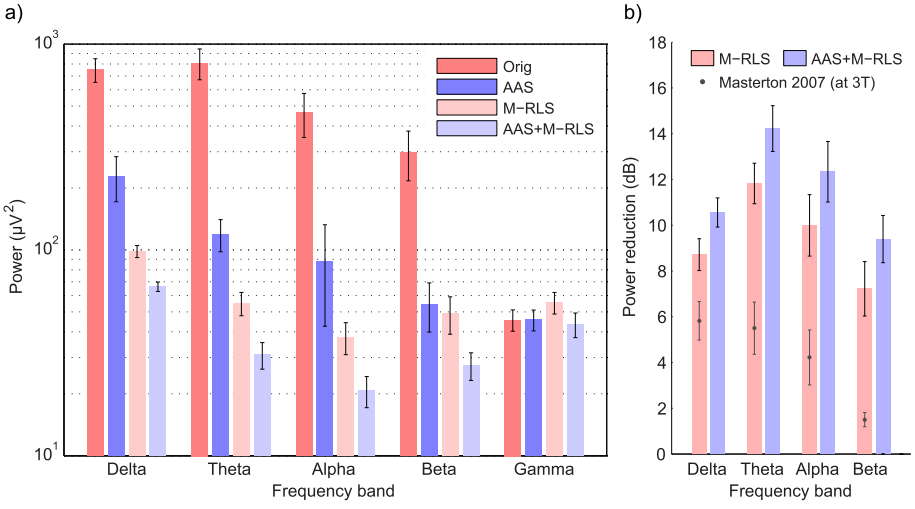

Fig. 2. The impact of AAS-based pulse artifact correction and M-RLS motion artifact correction on EEG signal power, after gradient artifact correction. a) Average EEG power per frequency band, before correction and after AAS, M-RLS, or AAS followed by M-RLS. b) Relative power reduction achieved with M-RLS or with AAS followed by M-RLS, relative to pre-processed, uncorrected data; values obtained in a previous study using M-RLS at 3 T (Masterton et al., 2007), without prior AAS, are included for comparison. Bar heights represent averages across channels and subjects, and error bars represent the standard error across subjects.

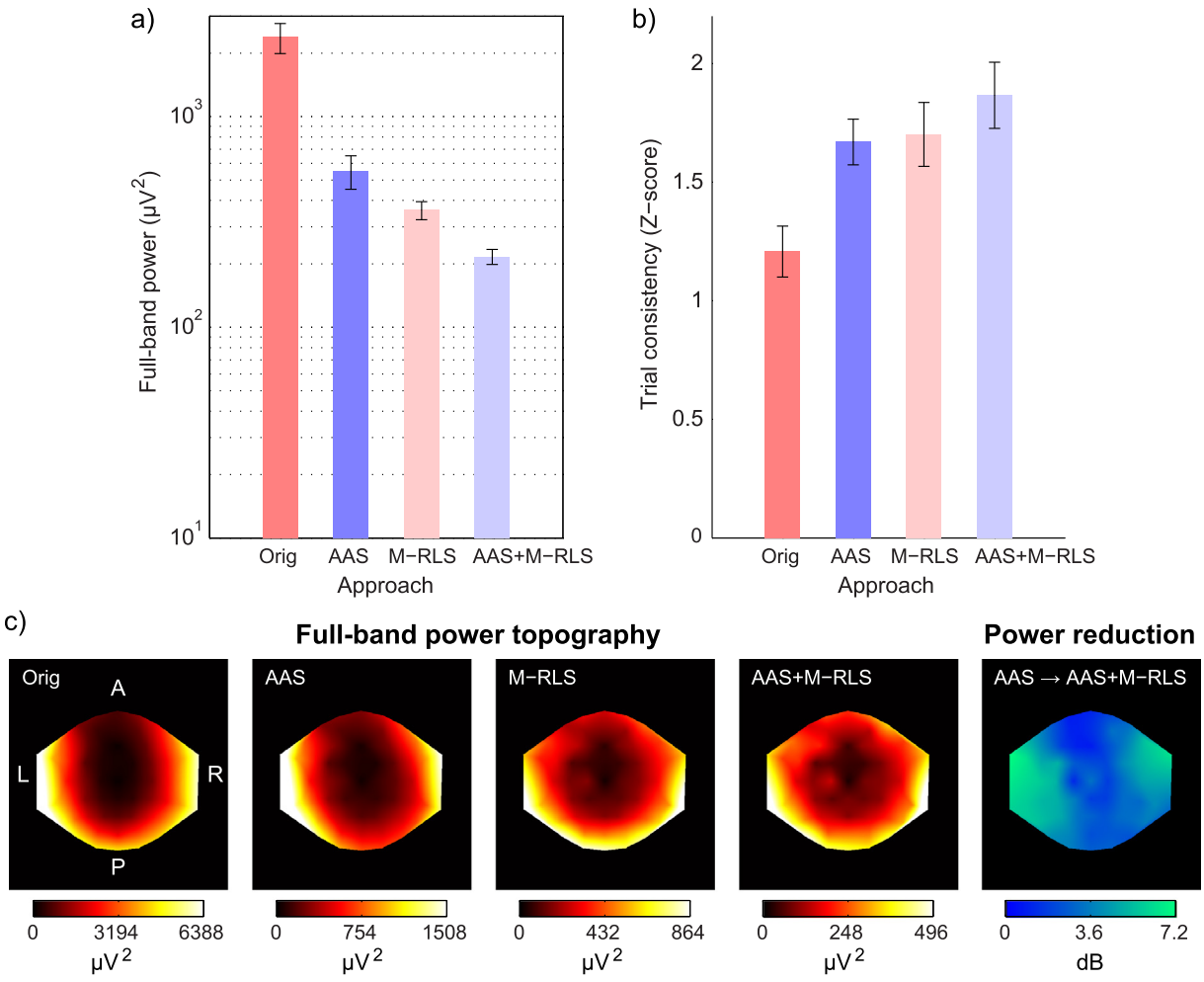

Fig. 3. The impact of AAS-based pulse artifact correction and M-RLS motion artifact correction on a) EEG signal power and b) VEP trial consistency, after gradient artifact correction. Bar heights represent averages across channels and subjects, and error bars represent the standard error across subjects. c) Subject-averaged full-band power topographies before (Orig) and after corrections (AAS, M-RLS, AAS + M-RLS), and the relative power reduction achieved with M-RLS after AAS correction.

the average Z-score was increased by 12 ± 11% with miICA, 37 ± 15% with ICA, 62 ± 17% with oM-RLS, and 86 ± 19% with oM-RLS followed by ICA (Fig. 6b). The value achieved with the combined approach was significantly higher than with miICA and oM-RLS alone, and tended to be superior to ICA as well ($p = 0.06$). The outcome of oM-RLS alone was significantly superior to that of miICA and, on average, also tended to be superior to ICA.

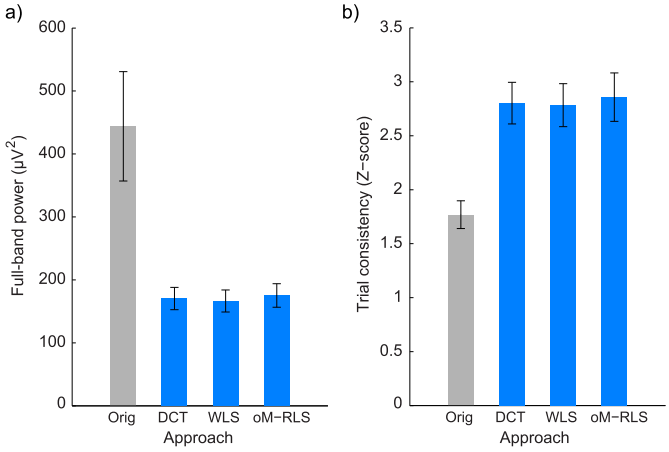

Fig. 4. The impact of motion artifact correction on a) EEG signal power and b) VEP trial consistency, after gradient and AAS-based pulse artifact correction. The techniques tested included DCT-based BLS, sliding-window WLS and oM-RLS. Bar heights represent averages across channels and subjects, and error bars represent the standard error across subjects.

Besides group-average effects, motion artifact correction also yielded clear improvements on visual response quality for each individual subject (Fig. 7, and remaining subjects in Supplementary Fig. 4). In several cases, oM-RLS effectively enabled the recovery of the main expected features of the VEP response, including the larger P100 component and even the more subtle N75 and N140 components. Scalp topographies at the timing of the P100 component were also improved considerably, showing a clearer anterior–posterior dipole and minimal left-to-right asymmetries. While trial-average responses were more drastically corrected in lateral channels, single-trial responses were still visibly improved in occipital channels, allowing for the detection of P100, N75 and N140 components in a large fraction of trials. The use of ICA after oM-RLS further added smaller, yet important benefits to signal quality, especially at a single-trial level (Fig. 7).

Discussion

In the present work, a novel technique for online measurement of EEG head motion artifacts was developed and implemented for simultaneous EEG-fMRI acquisitions at 7 T. Data were collected from 6 healthy subjects, and several aspects of post-processing artifact reduction methodology were analyzed, aiming for optimal data quality improvements

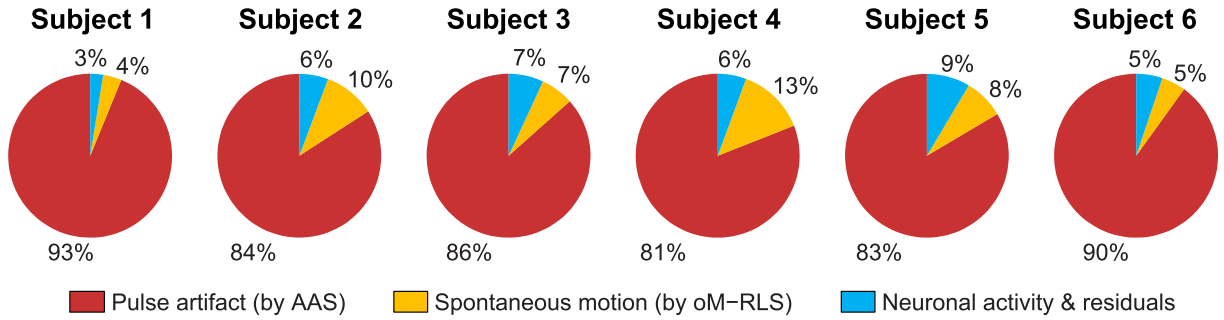

Fig. 5. EEG signal power distribution after gradient artifact correction, based on AAS pulse artifact correction and oM-RLS motion artifact correction. The percentages shown for each subject correspond to averages across EEG channels. As should be noted, these estimates were obtained based on the outcome of the artifact correction procedures, and as such are not perfect; in particular, the estimates for spontaneous motion contributions are expected to contain residuals of pulse artifacts, and vice versa.

using the motion information. The impact of spontaneous motion artifacts on EEG data at 7 T was for the first time quantitatively assessed, and significant improvements in visual response sensitivity were achieved with artifact reduction.

Motion artifact detection

The impact of spontaneous head motion on EEG recordings performed in strong magnetic fields is a well-known problem in EEG-fMRI studies (Flanagan et al., 2009; Jansen et al., 2012), most often addressed simply by excluding affected periods from data analysis, and in the worst cases discarding entire datasets. This approach incurs losses in acquisition time and costs, and tends to become less effective in acquisitions performed at higher magnetic fields. As discussed here (Introduction and Motion artifact generation sections) and in previous studies (Debener et al., 2008; Yan et al., 2010), motion artifacts are based on magnetic induction effects that scale with B_0. In this work, at 7 T, we estimated that contributions to signal variance from spontaneous motion artifacts are comparable to or even larger than those of actual neuronal activity (Fig. 5). The main artifact contributions were associated with the MRI gradients and the cardiac cycle, but while these contributions are approximately periodic, and thus more suited to temporal segmentation for averaging and subtraction, spontaneous motion does not follow regular patterns, and can thus highly benefit from an external monitoring system.

Several approaches for head motion detection have been proposed, including the use of highly sensitive optical systems (Maclaren et al., 2012), piezoelectric sensors (Bonmassar et al., 2002), and conductive wire loops (Masterton et al., 2007). We opted for loop-based sensors since they share similar mechanisms of artifact generation with EEG loops, and can be directly incorporated in linear regression models for EEG signal correction (as shown in the Motion artifact generation section). Optical systems, in contrast, while yielding more direct measures of head motion, would require the development of potentially complex forward models to estimate the resulting artifacts induced in each EEG loop. Similar to Masterton et al. (2007), we use multiple conductive loops distributed across the scalp, but while their approach uses a separate acquisition and recording system for the loops, we have implemented these sensors by adapting a number of electrodes from the EEG cap. This approach is not limited for use at 7 T, and requires neither additional amplification, gel layers or other recording equipment, nor modifications to the existing amplifiers, which are often the most expensive component of the EEG setup. While the cap adaptations, as implemented in this study, were non-permanent and set in place during each cap preparation, we foresee no impediments in the design of new cap models with these modifications permanently integrated. In particular, based on the tests conducted with our implementation, a modification with a similar number of sensors and resistor types is expected to have a negligible impact on either EEG or fMRI data quality. As a benefit, a permanent modification would not only save preparation time but also allow for a more geometrically optimal placement of the sensors (Abbott et al., 2014), which here was limited to the positions of the existing EEG electrodes. It should be noted that these sensors are connected to the reference electrode, and are thus not electrically isolated from the scalp. As such, an additional resistor was included in each connection to ensure subject safety, resulting in a total resistance of 25 kΩ for each motion loop (considering the two 5 kΩ resistors inserted in each channel lead), not including the resistance of gel interfaces between electrodes. It is also important that the input impedance of the amplifiers is sufficiently high to ensure that currents in the leads created by true neuronal activity are effectively negligible, so that the potential difference measured between each motion sensor and the reference will effectively comprise only magnetic induction effects.

Finally, since under certain assumptions EEG artifacts due to rigid-body head motion only depend on two degrees of freedom (head rotations, as described in the Motion artifact generation section), we point out that motion artifact reduction could potentially be performed using only two independent sensors. As in previous studies (Luo et al., 2014; Masterton et al., 2007), we have instead opted for an "overdetermined" detection approach, to ensure more robust estimations and for a higher sensitivity to eventual non-rigid motion effects — with the disadvantage of leaving less electrodes for actual EEG recording. Future studies may focus on the optimization of both the number and position of motion loops, possibly based on numerical simulations (Mullinger et al., 2014; Yan et al., 2010), towards the design of optimally effective motion sensor loops. We also stress the

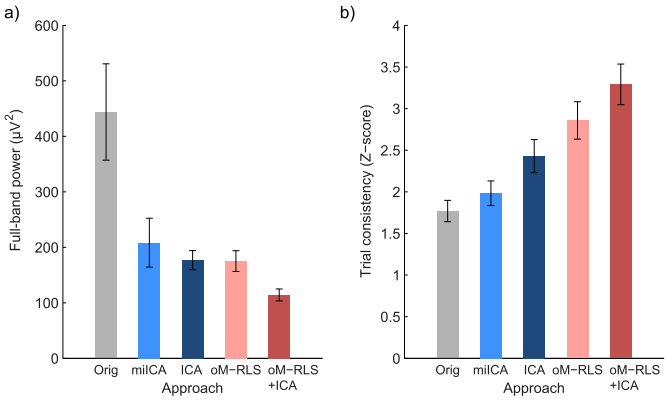

Fig. 6. The impact of ICA denoising and oM-RLS motion artifact correction on a) EEG signal power and b) VEP trial consistency, after gradient and AAS-based pulse artifact correction. The approaches tested comprised ICA, with and without including the motion sensor timecourses (milCA, ICA), oM-RLS, and oM-RLS followed by ICA. Bar heights represent averages across channels and subjects, and error bars represent the standard error across subjects.

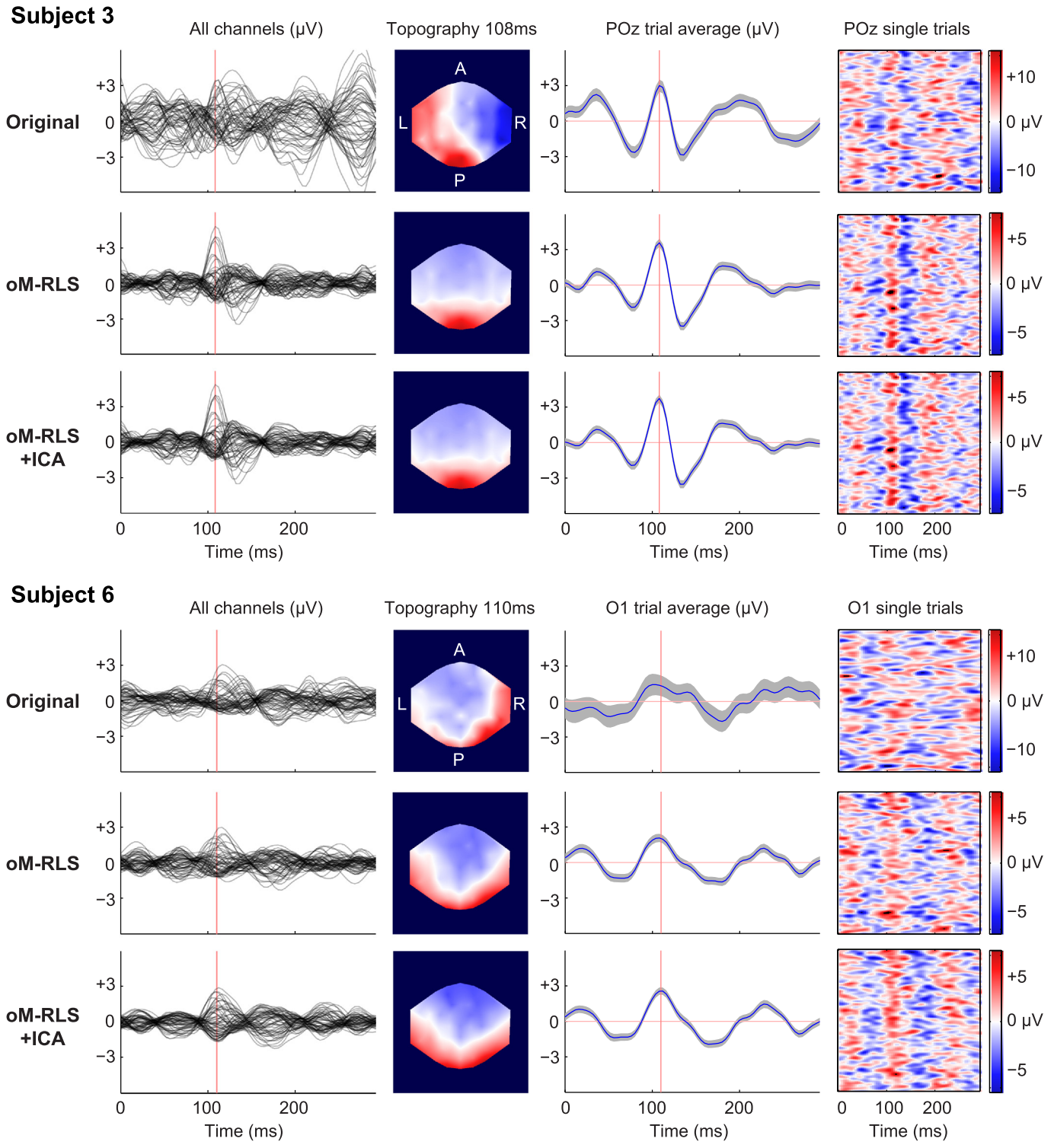

Fig. 7. EEG responses to visual stimulation with reversing checkerboards, in two subjects, before and after correction with oM-RLS, and with oM-RLS followed by ICA. In Subject 3, motion artifact correction provided the largest quality improvements, while in Subject 6 the benefits added by ICA were also considerably relevant. The scalp topographies shown correspond to the P100 component of the VEP, and are presented in a blue–white–red color scale centered at 0 V, with symmetric limits. The shaded margins in single-channel trial-averaged responses (3rd column) indicate the standard error across trials; the channel displayed was selected for having the largest average P100 amplitude amongst the occipital channels. Single-trial responses are shown Gaussian-smoothed across trials ($\sigma = 3$ trials).

importance of minimizing noise contributions at the transmission stage between the cap and amplifiers, as these sources do not follow rigid-body properties. In our setup, such contributions have been minimized by appropriate cable shortening and bundling, as described elsewhere (Jorge et al., 2015).

Motion artifact correction

Motion information can be used in various ways for data analysis, a simple and direct option being to use the sensor timecourses as an independent measure of head motion, which can guide epoch exclusion and

help determining whether particular fluctuations can effectively be attributed to neuronal activity (Abbott et al., 2014). Here, the sensor timecourses were used to reduce motion contributions throughout the EEG timecourses. The linear relationships between the artifacts captured by loop sensors and EEG channels (as described in the Motion artifact generation section) render them particularly suitable for linear regression methods, which were systemically explored in this work, in line with previous studies (Luo et al., 2014; Masterton et al., 2007). It should be noted that this type of approach relies on the assumption that motion artifacts are uncorrelated with neuronal activity (which forms the residuals of the linear fit). This assumption may become compromised in studies involving motor tasks, painful stimulation or attention modulations, for example, where subject motion may be more strongly correlated with the paradigm. Also important, as the weights of the linear relationships depend on the current head position (Eq. (4)), these linear models incorporated temporally-adaptive coefficients (Eq. (5)). The approaches here tested assume these coefficients to vary smoothly, and are thus less precise in the presence of large abrupt motion. Conversely, if the coefficients are allowed to adapt too quickly, the estimation may instead become significantly biased by neuronal activity. We opted to circumvent this compromise by rejecting the periods of most abrupt motion from data analysis, based on GFP fluctuations. The denoising of such periods would possibly require the use of other methods such as reference layer subtraction, where each electrode has a "copy" placed in the same position but connected to a reference layer, and denoising is performed with a direct signal subtraction, instead of a fit (Chowdhury et al., 2014). This could also be a potentially effective alternative for studies in which motion is expected to strongly correlate with brain activity. On the other hand, this approach requires twice as many recording channels, along with an additional gel layer, and residuals may still persist due to differences in the current paths across the scalp and across the reference layer; the additional (conductive) components are also more likely to affect MRI data quality (Mullinger et al., 2008b).

An important question investigated in this work regarded the combination of motion and pulse artifact correction (part I). In our subject group, the use of an AAS-based pulse artifact correction step followed by a motion sensor-based correction step was found to be more effective than either of the two techniques alone (Fig. 3). Consistent with this, while several studies have assumed the pulse artifact to be mainly caused by bulk head rotation, proposing to reduce both artifact types with motion sensors (Bonmassar et al., 2002; Luo et al., 2014; Masterton et al., 2007), substantial evidence exists for additional contributions to the pulse artifact, including local scalp dilations due to arterial pulsation, and the Hall effect occurring in charged particles carried by the blood as it flows in B_0 (Debener et al., 2008; Tenforde et al., 1983). In particular, the Hall effect has evinced more important contributions to pulse artifact variability than head rotation per se, at 3 T (Mullinger et al., 2013), and all three contributions are expected to scale with field strength. Our results suggest that the additional sources of the pulse artifact do create important contributions at 7 T, which should be addressed with a dedicated correction step. At lower fields, some caution should be taken with this approach, since the prior reduction of pulse artifacts leaves the linear fitting essentially dependent on spontaneous motion fluctuations alone, which at such field strengths may not be sufficiently strong for a robust, unbiased fit (given that brain activity does not scale with B_0, and its correlation with motion is never exactly null). The choice of a dedicated correction should thus be carefully considered depending on the field strength and the performance of each subject group.

Having settled for including a dedicated pulse artifact correction step, we then focused on determining optimal methods to tackle the contributions from spontaneous motion (part II). The three approaches tested led to similar outcomes in data denoising (Fig. 4), but do differ from each other in several aspects. Regarding computational speed, for comparison purposes, in our particular system and implementations (no parallelization added), BLS took less than 2 s to process each 5 min-long, 59-channel dataset, while oM-RLS took approximately 40 min, and WLS took more than 2 h. BLS is by far the fastest method and thus most suitable for exploratory tests and model optimization (the FIR kernel, for example); on the other hand, being based on parametric modeling, its adaptability depends on particular dataset properties such as the timecourse length. Sliding-window WLS avoids that limitation and relies on an intuitive adaptability parameter (the window FWHM), but was found to be considerably slower (although parallelization techniques could be applied both across channels and time). Finally, oM-RLS is a non-parametric technique based on a previously validated method for EEG data correction (Masterton et al., 2007), and provided a good compromise between versatility and computational speed, thus motivating our preference for this method. Additionally, the original M-RLS can be used for real-time correction.

Motion artifacts and ICA

The third part of this study compared the performance of motion sensor-based correction with that of ICA denoising, and investigated the benefits of combining the two techniques. ICA is often employed for EEG data analysis and denoising, both in pure EEG studies (Makeig et al., 1996; Onton et al., 2006) and with EEG-fMRI (Arrubla et al., 2013; Marques et al., 2009). In the second case, however, a number of authors have obtained suboptimal results with this approach, especially at fields above 1.5 T (Debener et al., 2007; Jorge et al., 2015). Similarly, our tests with ICA denoising alone systematically showed inferior results to those obtained with ICA after oM-RLS (Fig. 6), even with prior pulse correction applied in both cases. Without oM-RLS, the ICA component explaining the most variance was consistently found to be motion-related, with a left-to-right dipolar topography and low stimulus-locked periodicity. Nevertheless, the components associated with visual responses had considerably lower SNR than those obtained after oM-RLS, appearing to be still significantly contaminated with motion artifact contributions. Analogous results were found with miICA, where components attributed to the visual responses frequently exhibited appreciable projections on the motion channels. These issues are currently thought to be due to a violation of source stationarity, one of ICA's most important assumptions: while neuronal sources are measured as stationary (as long as the electrodes retain their positions on the scalp), motion-related artifacts are not. The pulse artifact, for instance, has been shown to increase in both amplitude and spatial variability with field strength (Debener et al., 2008), and our own theoretical description of motion artifacts (Motion artifact generation section) clearly shows their dependence on the current head position, thus varying their topography as head position drifts in time.

Despite the suboptimal performance obtained with ICA alone, its application following oM-RLS improved data quality. This is not unexpected since motion artifact correction does not cover other typical EEG artifacts (ocular movements, for example), which ICA can effectively isolate. Overall, for the 7 T datasets analyzed in this work, the combination of AAS-based pulse artifact correction, oM-RLS motion artifact correction and ICA denoising yielded optimal improvements in EEG data quality, with well appreciable benefits for visual response sensitivity. These were not only indicated by signal power and trial consistency measures, but also confirmed by direct observation of single subject results, both at trial-average and single-trial levels (Fig. 7, Supplementary Fig. 4). Motion artifact correction had a stronger impact on more lateral electrodes (Fig. 3c), as could be expected since the respective loops have the largest projection areas relative to B_0. Nevertheless, occipital channels still exhibited crucial improvements at a single-trial level, setting a highly encouraging quality mark for this multimodal approach at ultra-high field. Further improvements can be contemplated, for instance through the design of more unified correction schemes that can incorporate gradient, pulse and motion artifact estimation simultaneously — since head motion changes the projection of EEG loops

relative to B_0, it is thereby highly interconnected with the temporal variability of gradient and pulse artifacts, and the three could potentially be more effectively corrected together (Abbott et al., 2014).

Conclusion

The present study demonstrates clear improvements in EEG data quality acquired simultaneously with fMRI, at 7 T, through the minimization of motion-induced artifacts using information from independent loop sensors. At this field strength, spontaneous motion contributions to EEG signal variance were found to be comparable to or even larger than those of neuronal activity, and their removal led to strong improvements in the detection of visual responses, particularly at a single-trial level. Overall, we conclude that concurrent monitoring of head motion during simultaneous EEG-fMRI, along with the use of optimized data analysis techniques, can be highly beneficial for EEG data denoising, especially for studies conducted at higher magnetic field strengths.

Supplementary data to this article can be found online at http://dx.doi.org/10.1016/j.neuroimage.2015.07.020.

Acknowledgments

This work was supported by Centre d'Imagerie BioMédicale (CIBM) of the UNIL, UNIGE, HUG, CHUV, EPFL and the Leenaards and Jeantet Foundations, and by the Portuguese Science Foundation (FCT) through grants SFRH/BD/51449/2011, PTDC/EEI-ELC/3246/2012 and PEst-OE/EEI/LA0009/2013.

References

Abbott, D.F., Masterton, R.A., Archer, J.S., Fleming, S.W., Warren, A.E., Jackson, G.D., 2014. Constructing carbon fiber motion-detection loops for simultaneous EEG-fMRI. Front. Neurol. 5, 260.

Allen, P.J., Polizzi, G., Krakow, K., Fish, D.R., Lemieux, L., 1998. Identification of EEG events in the MR scanner: the problem of pulse artifact and a method for its subtraction. Neuroimage 8, 229–239.

Allen, P.J., Josephs, O., Turner, R., 2000. A method for removing imaging artifact from continuous EEG recorded during functional MRI. Neuroimage 12, 230–239.

Arrubla, J., Neuner, I., Hahn, D., Boers, F., Shah, N.J., 2013. Recording visual evoked potentials and auditory evoked P300 at 9.4 T static magnetic field. PLoS One 8, e62915.

Babiloni, F., Mattia, D., Babiloni, C., Astolfi, L., Salinari, S., Basilisco, A., Rossini, P.M., Marciani, M.G., Cincotti, F., 2004. Multimodal integration of EEG, MEG and fMRI data for the solution of the neuroimage puzzle. Magn. Reson. Imaging 22, 1471–1476.

Bonmassar, G., Purdon, P.L., Jaaskelainen, I.P., Chiappa, K., Solo, V., Brown, E.N., Belliveau, J.W., 2002. Motion and ballistocardiogram artifact removal for interleaved recording of EEG and EPs during MRI. Neuroimage 16, 1127–1141.

Bouchard, M., Quednau, S., 2000. Multichannel recursive-least-square algorithms and fast-transversal-filter algorithms for active noise control and sound reproduction systems. IEEE Trans. Speech Audio Process. 8, 606–618.

Chowdhury, M.E., Mullinger, K.J., Glover, P., Bowtell, R., 2014. Reference layer artefact subtraction (RLAS): a novel method of minimizing EEG artefacts during simultaneous fMRI. Neuroimage 84, 307–319.

Da Costa, S., van der Zwaag, W., Marques, J.P., Frackowiak, R.S., Clarke, S., Saenz, M., 2011. Human primary auditory cortex follows the shape of Heschl's gyrus. J. Neurosci. 31, 14067–14075.

Debener, S., Ullsperger, M., Siegel, M., Engel, A.K., 2006. Single-trial EEG-fMRI reveals the dynamics of cognitive function. Trends Cogn. Sci. 10, 558–563.

Debener, S., Strobel, A., Sorger, B., Peters, J., Kranczioch, C., Engel, A.K., Goebel, R., 2007. Improved quality of auditory event-related potentials recorded simultaneously with 3-T fMRI: removal of the ballistocardiogram artefact. Neuroimage 34, 587–597.

Debener, S., Mullinger, K.J., Niazy, R.K., Bowtell, R.W., 2008. Properties of the ballistocardiogram artefact as revealed by EEG recordings at 1.5, 3 and 7 T static magnetic field strength. Int. J. Psychophysiol. 67, 189–199.

Dempsey, M.F., Condon, B., Hadley, D.M., 2001. Investigation of the factors responsible for burns during MRI. J. Magn. Reson. Imaging 13, 627–631.

Eichele, T., Specht, K., Moosmann, M., Jongsma, M.L., Quiroga, R.Q., Nordby, H., Hugdahl, K., 2005. Assessing the spatiotemporal evolution of neuronal activation with single-trial event-related potentials and functional MRI. Proc. Natl. Acad. Sci. U. S. A. 102, 17798–17803.

Fan, J., Zhang, W., 2000. Simultaneous confidence bands and hypothesis testing in varying-coefficient models. Scand. J. Stat. 27, 715–731.

Flanagan, D., Abbott, D.F., Jackson, G.D., 2009. How wrong can we be? The effect of inaccurate mark-up of EEG/fMRI studies in epilepsy. Clin. Neurophysiol. 120, 1637–1647.

Gotman, J., Pittau, F., 2011. Combining EEG and fMRI in the study of epileptic discharges. Epilepsia 52 (Suppl. 4), 38–42.

Hill, R.A., Chiappa, K.H., Huang-Hellinger, F., Jenkins, B.G., 1995. EEG during MR imaging: differentiation of movement artifact from paroxysmal cortical activity. Neurology 45, 1942–1943.

Hoover, D.R., Rice, J.A., Wu, C.O., Yang, L.-P., 1998. Nonparametric smoothing estimates of time-varying coefficient models with longitudinal data. Biometrika 85, 809–822.

Huang, J.Z., Wu, C.O., Zhou, L., 2002. Varying-coefficient models and basis function approximations for the analysis of repeated measurements. Biometrika 89, 111–128.

Jansen, M., White, T.P., Mullinger, K.J., Liddle, E.B., Gowland, P.A., Francis, S.T., Bowtell, R., Liddle, P.F., 2012. Motion-related artefacts in EEG predict neuronally plausible patterns of activation in fMRI data. Neuroimage 59, 261–270.

Jorge, J., Figueiredo, P., van der Zwaag, W., Marques, J.P., 2013. Signal fluctuations in fMRI data acquired with 2D-EPI and 3D-EPI at 7 Tesla. Magn. Reson. Imaging 31, 212–220.

Jorge, J., van der Zwaag, W., Figueiredo, P., 2014. EEG-fMRI integration for the study of human brain function. Neuroimage 102 (Pt 1), 24–34.

Jorge, J., Grouiller, F., Ipek, Ö., Stoermer, R., Michel, C.M., Figueiredo, P., van der Zwaag, W., Gruetter, R., 2015. Simultaneous EEG-fMRI at ultra-high field: artifact prevention and safety assessment. Neuroimage 105, 132–144.

Kim, H.C., Yoo, S.S., Lee, J.H., 2015. Recursive approach of EEG-segment-based principal component analysis substantially reduces cryogenic pump artifacts in simultaneous EEG-fMRI data. Neuroimage 104, 437–451.

Lee, T.W., Girolami, M., Sejnowski, T.J., 1999. Independent component analysis using an extended infomax algorithm for mixed subgaussian and supergaussian sources. Neural Comput. 11, 417–441.

Lemieux, L., Allen, P.J., Franconi, F., Symms, M.R., Fish, D.R., 1997. Recording of EEG during fMRI experiments: patient safety. Magn. Reson. Med. 38, 943–952.

Luo, Q., Glover, G.H., 2012. Influence of dense-array EEG cap on fMRI signal. Magn. Reson. Med. 68, 807–815.

Luo, Q., Huang, X., Glover, G.H., 2014. Ballistocardiogram artifact removal with a reference layer and standard EEG cap. J. Neurosci. Methods 233, 137–149.

Maclaren, J., Armstrong, B.S., Barrows, R.T., Danishad, K.A., Ernst, T., Foster, C.L., Gumus, K., Herbst, M., Kadashevich, I.Y., Kusik, T.P., Li, Q., Lovell-Smith, C., Prieto, T., Schulze, P., Speck, O., Stucht, D., Zaitsev, M., 2012. Measurement and correction of microscopic head motion during magnetic resonance imaging of the brain. PLoS One 7, e48088.

Makeig, S., Bell, A.J., Jung, T.P., Sejnowski, T.J., 1996. Independent component analysis of electroencephalographic data. Adv. Neural Inf. Process. Syst. 8 (8), 145–151.

Marques, J.P., Rebola, J., Figueiredo, P., Pinto, A., Sales, F., Castelo-Branco, M., 2009. ICA decomposition of EEG signal for fMRI processing in epilepsy. Hum. Brain Mapp. 30, 2986–2996.

Masterton, R.A., Abbott, D.F., Fleming, S.W., Jackson, G.D., 2007. Measurement and reduction of motion and ballistocardiogram artefacts from simultaneous EEG and fMRI recordings. Neuroimage 37, 202–211.

Mullinger, K., Bowtell, R., 2011. Combining EEG and fMRI. Methods Mol. Biol. 711, 303–326.

Mullinger, K., Brookes, M., Stevenson, C., Morgan, P., Bowtell, R., 2008a. Exploring the feasibility of simultaneous electroencephalography/functional magnetic resonance imaging at 7 T. Magn. Reson. Imaging 26, 968–977.

Mullinger, K., Debener, S., Coxon, R., Bowtell, R., 2008b. Effects of simultaneous EEG recording on MRI data quality at 1.5, 3 and 7 Tesla. Int. J. Psychophysiol. 67, 178–188.

Mullinger, K.J., Havenhand, J., Bowtell, R., 2013. Identifying the sources of the pulse artefact in EEG recordings made inside an MR scanner. Neuroimage 71, 75–83.

Mullinger, K.J., Chowdhury, M.E., Bowtell, R., 2014. Investigating the effect of modifying the EEG cap lead configuration on the gradient artifact in simultaneous EEG-fMRI. Front. Neurosci. 8, 226.

Neuner, I., Arrubla, J., Felder, J., Shah, N.J., 2014. Simultaneous EEG-fMRI acquisition at low, high and ultra-high magnetic fields up to 9.4 T: perspectives and challenges. Neuroimage 102 (Part 1), 71–79.

Niazy, R.K., Beckmann, C.F., Iannetti, G.D., Brady, J.M., Smith, S.M., 2005. Removal of FMRI environment artifacts from EEG data using optimal basis sets. Neuroimage 28, 720–737.

Nierhaus, T., Gundlach, C., Goltz, D., Thiel, S.D., Pleger, B., Villringer, A., 2013. Internal ventilation system of MR scanners induces specific EEG artifact during simultaneous EEG-fMRI. Neuroimage 74, 70–76.

Noth, U., Laufs, H., Stoermer, R., Deichmann, R., 2012. Simultaneous electroencephalography-functional MRI at 3 T: an analysis of safety risks imposed by performing anatomical reference scans with the EEG equipment in place. J. Magn. Reson. Imaging 35, 561–571.

Onton, J., Westerfield, M., Townsend, J., Makeig, S., 2006. Imaging human EEG dynamics using independent component analysis. Neurosci. Biobehav. Rev. 30, 808–822.

Rothlubbers, S., Relvas, V., Leal, A., Figueiredo, P., 2013. Reduction of EEG artefacts induced by vibration in the MR-environment. Conf. Proc. IEEE Eng. Med. Biol. Soc. 2013, 2092–2095.

Tenforde, T.S., Gaffey, C.T., Moyer, B.R., Budinger, T.F., 1983. Cardiovascular alterations in Macaca monkeys exposed to stationary magnetic fields: experimental observations and theoretical analysis. Bioelectromagnetics 4, 1–9.

van der Zwaag, W., Francis, S., Head, K., Peters, A., Gowland, P., Morris, P., Bowtell, R., 2009. fMRI at 1.5, 3 and 7 T: characterising BOLD signal changes. Neuroimage 47, 1425–1434.

Widmann, A., Schroger, E., Maess, B., 2015. Digital filter design for electrophysiological data — a practical approach. J. Neurosci. Methods 250, 34–46.

Yacoub, E., Harel, N., Ugurbil, K., 2008. High-field fMRI unveils orientation columns in humans. Proc. Natl. Acad. Sci. U. S. A. 105, 10607–10612.

Yan, W.X., Mullinger, K.J., Brookes, M.J., Bowtell, R., 2009. Understanding gradient artefacts in simultaneous EEG/fMRI. Neuroimage 46, 459–471.

Yan, W.X., Mullinger, K.J., Geirsdottir, G.B., Bowtell, R., 2010. Physical modeling of pulse artefact sources in simultaneous EEG/fMRI. Hum. Brain Mapp. 31, 604–620.